Chapter 2

Experimental Methods

In this chapter, theoretical aspects and the experimental set up of He atom scattering (HAS), low energy electron diffraction (LEED), and scanning tunneling microscopy (STM) are discussed. All three techniques are capable of determining the structure of single crystal surfaces. The diffraction experiments determine the symmetry and dimension of unit cell as well as the scattering centers in the unit cell via the angular and intensity distributions of diffraction beams. Tunneling microscopy, on the other hand, directly probes the surface in real space and provides information on local morphology in atomic scale in contrast to diffraction, which relies on long range order of the surface.

Helium atom scattering is a powerful tool to investigate exclusively the topmost surface layer. In this technique, the surface is probed by neutral He atoms with a very low kinetic energy (10-65 meV). Helium atoms in this energy range have a de Broglie wave length comparable to the lattice spacing. Scattered He atoms thus exhibit interference effects. Due to the very low kinetic energy of the He atoms, the surface is probed nondestructively. Furthermore, HAS is a useful technique to investigate imperfections on the surfaces. Because of the large He atom scattering cross section of all kinds of defects like adatoms, vacancies, etc., their presence on the surface causes a significant decrease in the intensity of the reflected He atom beam. This technique is also capable of providing information on step heights and terrace widths. Apart from these investigations by elastic He scattering, low energy surface vibrations can be studied by inelastic He scattering.

Low energy electron diffraction is the most common technique used in single crystal surface

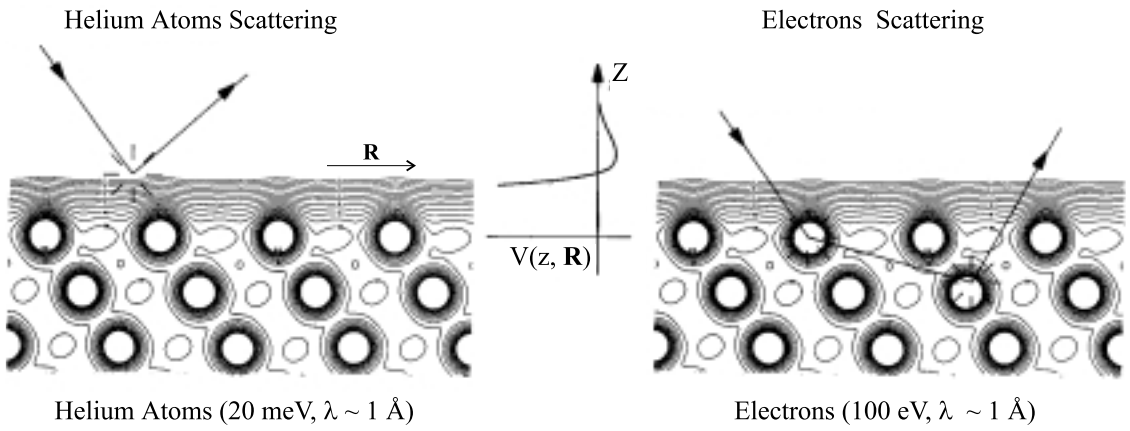

Figure 2.1: A schematic diagram elucidating the different nature of He atoms and electron scattering from the crystal surfaces. Electrons penetrate several Angstroms into the surface and undergo multiple scattering, whereas He atoms are reflected well above the surface [93].

investigations. In LEED electrons of energy 50-200 eV are used as a probe. In contrast to the He atoms reflecting well above the surface (2-3 Å) [92] due to the repulsive force of the electron cloud of the surface atoms, electrons penetrate a few atomic layers into the sample before being scattered from the atom potentials (see Figure 2.1), therefore yielding information about a few topmost monolayers.

Scanning tunneling microscopy was developed by G. Binnig, H. Rohrer, Ch. Gerber, and E. Weibel [94] in the eighties. This technique is based on the principle of quantum mechanical tunneling of electrons between a sharp tip and a surface, where the tunneling starts at a tip-surface separation of a few Angstroms. While scanning the tip across the sample surface, the tunneling current is measured, mapping the local electron density of the surface. STM and HAS can be considered as complementary techniques in the sense that the former gives information of the topmost layer in real space and the latter in reciprocal space.

There are many books and review articles published on all three techniques. References [95-97] deal with theoretical and experimental aspects of He atom scattering, while the recent article by Farías *et al.* [92] gives a review of the diffractive phenomena on surfaces studied by He diffraction. One can refer to Ref. [98, 99] for details about low energy electron diffraction. The fundamental principle and application of scanning tunneling microscopy is cited in Ref. [100].

2.1 Helium Atom Scattering

2.1.1 Theoretical Aspects of Elastic Scattering

Atom-Surface Potential

In describing atom scattering from surfaces, an atom-surface potential has to be established. The atom-surface potential can be divided into two parts, a long range attractive potential due to Van der Waals forces dominating at large separation and a short range repulsive potential arising from the exchange force (the Pauli principle), when the electron cloud of the atom overlaps with the valence electron density extending out of the solid. A qualitative picture of the atom-solid potential can be obtained by summing over the binary interaction potential between the incoming atom and individual atoms of the solid. Figure 2.2 shows the resulting atom-surface potential for a monoatomic solid [101] elucidating some important features of the atom-surface potential. The classical turning points of atoms impinging on a surface atom (B) are farther out compared to that of atoms coming in between them (A). This is reflected in a periodic modulation of the repulsive potential. The classical turning points form an equipotential surface described by the corrugation function $\zeta(\mathbf{R})$, where $\mathbf{R}$ denotes the vector in the surface plane.

The periodic modulation of the repulsive potential reflects the density of valence electrons

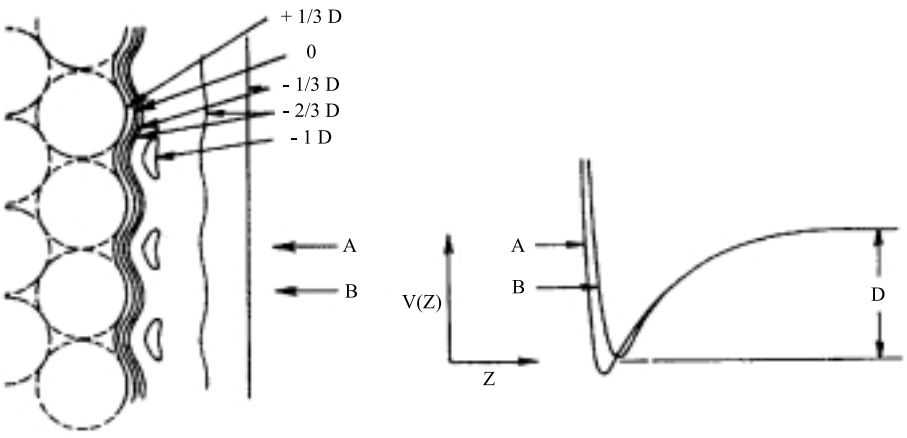

Figure 2.2: A schematic diagram illustrating the interaction of neutral atoms with a solid surface. The left shows the equipotential lines in term of depth of potential well (D) and the right displays the potential versus z, the direction perpendicular to the surface plane [101].

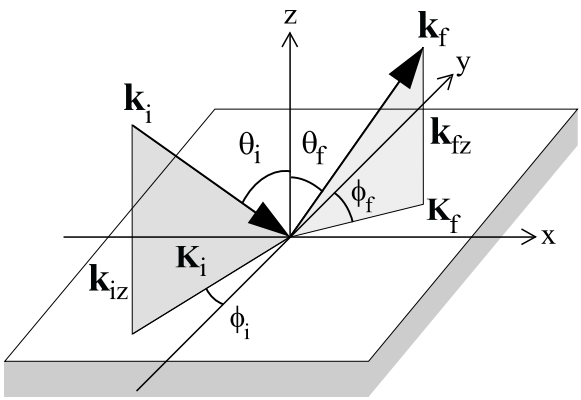

Figure 2.3: Definition of scattering geometry. For the in-plane scattering configuration, $\phi_i = \phi_f$.

of the surface atoms. For He atoms with energies less than 100 meV, a good approximation to the repulsive potential (V_{rep}) is [102]

$$V_{rep} = \alpha\rho(\mathbf{r}), \tag{2.1}$$

with $\rho(\mathbf{r})$ the electron density and α constant. In fact, alkali halides surfaces, which have highly localized valence electrons are experimentally found to have a high corrugation, while the metallic surfaces, where the valence electrons are smeared out parallel to the surface, have a very low corrugation (see for example [92]).

Diffraction Conditions

Consider a beam of He atoms with mass m and energy E_i impinging on a surface at an angle θ_i with surface normal. The de Broglie wavelength (λ_i) of atoms with energy E_i is given by,

$$\lambda_i = \frac{h}{\sqrt{2mE_i}}, \quad \lambda_i/\text{Å} = \frac{4.57}{\sqrt{E_i/\text{meV}}}, \tag{2.2}$$

h being Planck's constant. In diffraction experiments, He atoms with energy 10-65 meV are used so that λ_i ranges from 1.4 Å to 0.6 Å, which is comparable to the lattice spacing. The wave vector $\mathbf{k}_i$ of the impinging atoms relates to the wavelength λ_i by,

$$k_i = |\mathbf{k}_i| = \frac{2\pi}{\lambda_i}. \tag{2.3}$$

For in-plane scattering ($\phi_i = \phi_f$, see scattering geometry in Figure 2.3), the incident wave vector $\mathbf{k}_i$ can be decomposed into parallel and perpendicular components as,

$$\mathbf{k}_i = (\mathbf{K}_i, k_{iz}) \quad \text{with} \quad |\mathbf{K}_i| = k_i \sin\theta_i,\ k_{iz} = -k_i \cos\theta_i, \tag{2.4}$$

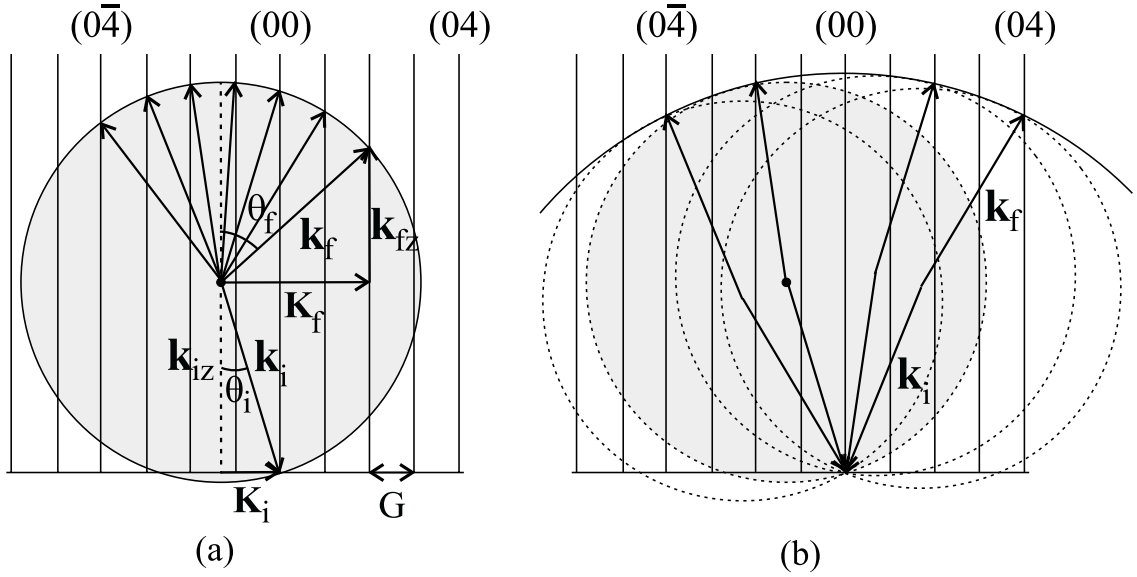

Figure 2.4: Ewald construction for elastic scattering from the 2D surface lattice. The point of intersection of the Ewald sphere (here circle) with the vertical rods determines the final wave vector $\mathbf{k}_f$. (a) for the scattering geometry with fixed θ_i and variable θ_f and (b) for fixed $\theta_i + \theta_f$, where both θ_i and θ_f are varied (see text in Section 2.2 for details).

z being perpendicular to the surface plane.

Two conditions have to be fulfilled for elastic scattering, the energy conservation,

$$k_i^2 = k_f^2 = K_f^2 + k_{fz}^2, \tag{2.5}$$

and the parallel momentum conservation,

$$\mathbf{K}_i + \mathbf{G} = \mathbf{K}_f, \tag{2.6}$$

where $\mathbf{k}_f = (\mathbf{K}_f, k_{fz})$, with $|\mathbf{K}_f| = k_f \sin\theta_f$, $k_{fz} = -k_f \cos\theta_f$, is the wave vector of outgoing atom and $\mathbf{G} = n_1\mathbf{b}_1 + n_2\mathbf{b}_2$ (n_1, n_2 are integers) is a surface reciprocal lattice vector, which is related to the unit cell vectors $\mathbf{a}_1$ and $\mathbf{a}_2$ by

$$\mathbf{a}_i.\mathbf{b}_j = 2\pi\delta_{ij}, \quad (i,j = 1,2). \tag{2.7}$$

Equation 2.6 is the Bragg condition in two dimensions. The conditions given by Equations 2.5 and 2.6 can be represented graphically by the Ewald construction as shown in Figure 2.4.

Experimentally, the parallel momentum transfer ($\Delta k_{\|}$) is probed either by varying θ_f keeping θ_i fixed or by varying both θ_f and θ_i keeping $\theta_f + \theta_i$ fixed. For either case,

$$\Delta k_{\|} = k_i(\sin\theta_f - \sin\theta_i). \tag{2.8}$$

The value of the lattice constant a is determined from the n^{th} order diffraction peak by

$$\Delta k_{\|} = k_i(\sin\theta_f - \sin\theta_i) = \frac{2\pi}{a}n. \tag{2.9}$$

Calculation of Diffraction Intensity

Once the atom-surface model potential $V(r)$ is established, the scattering amplitudes or intensities can be evaluated by solving the Schrödinger equation,

$$-\frac{\hbar^2}{2m}\nabla^2\psi(r) + V(r)\psi(r) = E\psi(r). \tag{2.10}$$

The exact solution of the Schrödinger equation for a rigid periodic potential can be obtained by various methods (refer to [103] for a review). Here, some approximation methods, which are relevant to determining a corrugation function from diffraction data, are presented.

Hard Corrugated Wall (HCW) Method

The most convenient and physically plausible approximation method is the Hard Corrugated Wall (HCW), which was first introduced by Garibaldi *et al.* [104] in 1975. This method assumes the surface is an infinitely hard corrugated wall with the atom-surface potential expressed as,

$$V(\mathbf{R}, z) = \begin{cases} 0 & \text{for } z > \zeta(\mathbf{R}) \\ \infty & \text{for } z \leq \zeta(\mathbf{R}) \end{cases}. \tag{2.11}$$

The following assumptions about the atom-surface interaction potential are made in this method: (a) The attractive part of the potential is neglected. This assumption is reasonable if the energy of the incoming atoms is much larger than the attractive well depth ($E_i \gg D$). For He surface potentials, the value of D is normally between 5-10 meV [92], which is much less than the energy of He atoms in a room temperature ($\sim$ 60 meV). Hence, a room temperature He atoms beam satisfies the condition. For $E_i \sim D$, the attractive part can no longer be neglected because this case leads to the resonant scattering or selective adsorption (see Ref. [96] for selective adsorption), which will strongly influence the diffraction intensities. However, if

selective adsorption does not play a major role, the HCW method can be still used to calculate the diffraction intensities by employing a simple correction in θ_i and k_i [92, and find references therein],

$$\sin\theta_i' = \frac{|\mathbf{k}_i|}{|\mathbf{k}_i'|}\sin\theta_i = \frac{\sin\theta_i}{\sqrt{1+\frac{D}{E_i}}}. \tag{2.12}$$

Further assumptions are:

(b) The slope of the steeply rising part of the potential is assumed to be infinite.

(c) Lattice vibrations are neglected i.e. surface atoms are considered to be at rest.

Based on the HCW approach, several methods have been developed to calculate the diffraction intensities (for review see [96]).

Rayleigh Approximation

Consider a wave function $\psi(\mathbf{r})$ as proposed by Rayleigh [105], which assumes the incoming and outgoing waves are plane waves up to the surface. The total wave function is the wave function of incoming atoms plus the sum of plane waves of diffracted atoms,

$$\psi(\mathbf{R},z) = e^{i[\mathbf{K}_i.\mathbf{R}+k_{iz}z]} + \sum_{\mathbf{G}} A_{\mathbf{G}} e^{i[(\mathbf{K_i}+\mathbf{G}).\mathbf{R}+k_{fz}(\mathbf{G})z]}, \tag{2.13}$$

where $A_{\mathbf{G}}$ is the scattering amplitude and the summation extends over a finite set of $\mathbf{G}$ vectors corresponding to a finite number of propagating waves (for which k_{fz} is real, i.e., $k_{fz}^2 = k_i^2 - |\mathbf{K}+\mathbf{G}|^2 > 0$) and a infinite number of exponentially decaying waves (for imaginary k_{fz} i.e. $k_{fz}^2 = k_i^2 - |\mathbf{K}+\mathbf{G}|^2 < 0$). The intensity $P_{\mathbf{G}}$ of the propagating waves is calculated from the scattering amplitude by,

$$P_{\mathbf{G}} = \frac{|k_{fz}|}{|k_{iz}|}|A_{\mathbf{G}}|^2. \tag{2.14}$$

The intensities satisfy the unitary condition,

$$\sum_{\mathbf{G}} P_{\mathbf{G}} = 1. \tag{2.15}$$

To determine $A_{\mathbf{G}}$, the boundary condition $\psi(\mathbf{R}, z=\zeta(\mathbf{R})) = 0$ is used in Equation 2.13, which gives,

$$0 = e^{ik_{iz}\zeta(\mathbf{R})} + \sum_{\mathbf{G}} A_{\mathbf{G}} e^{i[\mathbf{G}.\mathbf{R}+k_{fz}(\mathbf{G})\zeta(\mathbf{R})]}. \tag{2.16}$$

Multiplication of Equation 2.16 by $e^{-ik_{iz}\zeta(\mathbf{R})}$ leads to,

$$\sum_{\mathbf{G}} A_{\mathbf{G}} M_{\mathbf{G},\mathbf{R}} = -1, \tag{2.17}$$

with

$$M_{\mathbf{G},\mathbf{R}} = e^{i[\mathbf{G}.\mathbf{R}+(k_{fz}(\mathbf{G})-k_{iz})\zeta(\mathbf{R})]}. \tag{2.18}$$

$A_{\mathbf{G}}$ can be obtained by solving Equation 2.17. Different methods can be employed to solve the equation. Among them the GR method and the eikonal approximation are widely used.

The GR Method: The GR method was first proposed by García [106]. The idea of the GR method is that Equation 2.17 can be solved numerically by taking certain discrete values of $\mathbf{R}$ distributed uniformly in the surface unit cell and the same number of $\mathbf{G}$ vectors uniformly distributed in reciprocal space so that the equation converts into a finite number of linear equations, which can be solved by matrix inversion. This method gives convergent solutions only for certain conditions. For instance, it is convergent for a 1D sinusoidal corrugation function of period a, $\zeta(x) = \frac{\zeta_m}{2}\sin\frac{2\pi x}{a}$, ($\zeta_m$ is the maximum corrugation amplitude) if $\zeta_m \leq 0.14\ a$.

Eikonal Approximation: An alternative method to solve Equation 2.16 is the eikonal approximation, which is based on the assumption that for small $\mathbf{G}$ ($G < k_i$), the term $e^{ik_{fz}(\mathbf{G})\zeta(\mathbf{R})}$ is a slowly varying function of $\mathbf{G}$ and can be taken out from the summation. Under this assumption, Equation 2.16 takes the form

$$\sum_{\mathbf{G}} A_{\mathbf{G}} e^{i\mathbf{G}.\mathbf{R}} = -e^{[(k_{iz}-k_{fz})\zeta(\mathbf{R})]}, \tag{2.19}$$

and $A_{\mathbf{G}}$ can be evaluated,

$$A_{\mathbf{G}} = -\frac{1}{S}\int_{u.c.} e^{-i\mathbf{G}.\mathbf{R}} e^{i[(k_{iz}-k_{fz})\zeta(\mathbf{R})]} d\mathbf{R}, \tag{2.20}$$

(S denotes the area of unit cell). $A_{\mathbf{G}}$ is simply the Fourier transform of a phase factor whose argument is the product of the known corrugation function and the perpendicular momentum transfer. For simple corrugation profiles Equation 2.20 can be solved analytically.

The eikonal approximation excludes multiple scattering and does not satisfy the unitary condition (Equation 2.15). However, the intensities calculated by this method can be very close to the exact calculation for suitable systems. Reasonable results can be obtained for $\zeta_m < 0.1\ a$ and $\theta_i < 45°$ [96].

The methods to calculate diffraction intensities explained so far consider the atoms at rest. In reality, thermal vibrations and the quantum mechanical zero-point motion of surface atoms leads to inelastic scattering reducing the diffraction intensities without changing the peak profiles. The influence of inelastic scattering is accounted for by multiplying the intensity (Equation 2.14) by a Debye-Waller factor,

$$F_{DW} = e^{-2W} \quad \text{with} \quad W = \frac{1}{2}\langle(\mathbf{u}\cdot\Delta\mathbf{k})^2\rangle, \tag{2.21}$$

where $\Delta\mathbf{k} = \mathbf{k}_f - \mathbf{k}_i$, $\mathbf{u}$ is the displacement of atoms from their equilibrium position, and $\langle\ldots\rangle$ denotes thermal averaging.

The GR and eikonal approximation methods give procedures to get diffraction intensities from a given corrugation function. In practice, the corrugation has to be determined from the experimental diffraction intensities. The direct inversion of experimental data is not possible because the phase information is lost in the measured intensities. Therefore, one has to follow a trial and error method. The Fourier amplitudes of $\zeta(\mathbf{R})$, which best fit the calculated and experimental data can be searched by monitoring the reliability factor,

$$R = \frac{1}{N}\sqrt{\sum_{\mathbf{G}}(P_{\mathbf{G}}^{Cal} - P_{\mathbf{G}}^{Exp})^2}. \tag{2.22}$$

2.1.2 Theoretical Aspects of Inelastic Scattering

Kinematics

During the phonon inelastic scattering of atoms from a periodic surface, the parallel momentum and the energy exchange takes place between the system and the incoming atoms due to phonon creation and annihilation. The dynamical theory requires the conservations of parallel momentum and the energy of the entire system. With energy and parallel momentum transfers ΔE and $\Delta\mathbf{K}$, respectively, energy and the momentum conservation can be expressed as,

$$\Delta E = E_f - E_i = \frac{\hbar^2 k_f^2}{2m} - \frac{\hbar^2 k_i^2}{2m} = \hbar\omega(\mathbf{Q}), \tag{2.23}$$

and

$$\Delta\mathbf{K} = \mathbf{K}_f - \mathbf{K}_i = \mathbf{Q} + \mathbf{G}, \quad \text{with} \quad |\mathbf{K}_f| = k_f \sin\theta_f,\ |\mathbf{K}_i| = k_i \sin\theta_i, \tag{2.24}$$

where $\omega(\mathbf{Q})$ is the phonon frequency and $\mathbf{Q}$ is the phonon momentum. A negative value of $\hbar\omega(\mathbf{Q})$ ($\Delta E < 0$) corresponds to phonon creation and a positive value ($\Delta E > 0$) to phonon

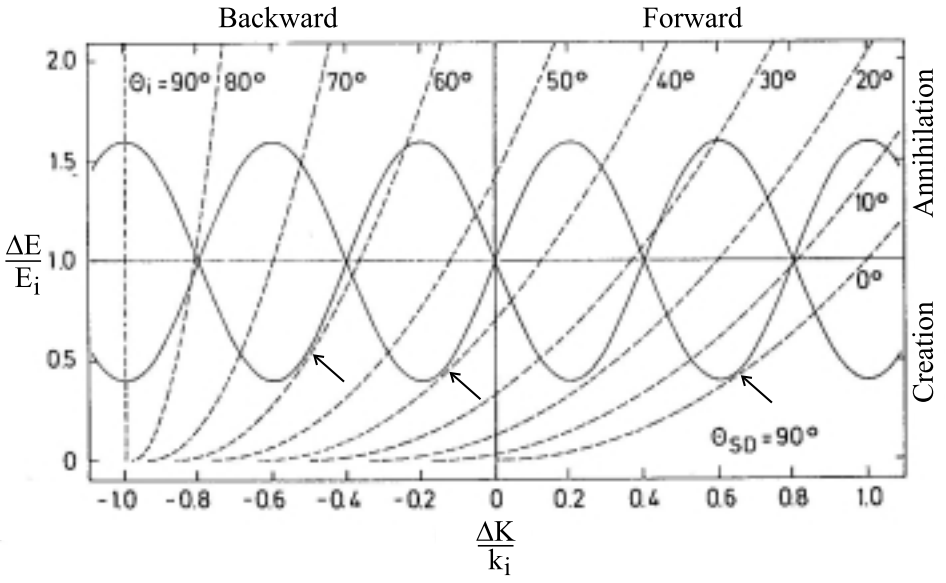

Figure 2.5: A set of scan curves for He scattering with fixed $\theta_i + \theta_f = 90°$ (dashed curves) and a possible Rayleigh mode dispersion curve (solid curve) in an extended zone plot.

annihilation. Similarly, a negative value of ΔK is referred to "backward-directed phonons" and a positive value to "forward-directed" phonons. Combination of Equations 2.23 and 2.24 yields

$$\frac{\Delta E}{E_i} = (\frac{\sin\theta_i + \Delta K/k_i}{\sin\theta_f})^2 - 1. \tag{2.25}$$

The plot of ΔE versus ΔK is a parabola with origin at ($-E_i, -K_i$) and the curvature of the parabola depends on k_i, θ_i and θ_f (see Figure 2.5). The plot is called scan curve, which is very useful to explain some important features of phonon excitations.

The intersections of the scan curve with the dispersion curves determine the values of ΔE at which the maxima are expected in the energy loss (or gain) spectra. As can be seen from Figure 2.5, a single scan curve in general intersects the dispersion curve in more than one point. This implies that it is possible to observe phonon creation/annihilation with backward-directed/forward-directed peaks in a single spectrum. The width of the phonon peak depends on the angle of intersection of the scan curve and the dispersion curve in addition to intrinsic width and broadening due to other experimental parameters. The spectra taken at particular angles θ_i have phonon peaks with optimum resolution if the scan curves corresponding to those θ_i intersect the dispersion curve at a right angle. The peaks are very broad at critical angles (θ_i^c) at which the two curves intersect tangentially (indicated by arrows in the figure). A small

change in θ_i from θ_i^c either causes the disappearance of peaks or generates two overlapping peaks. This mechanism is called kinematical focusing (first introduced in Ref. [107]). Furthermore, the scan curves passing through the first Brillouin zone cut the dispersion curves more steeply in the annihilation-backward or creation-forward quadrants, therefore probing the dispersion curve in these regions normally gives more pronounced phonon peaks.

Diffraction Intensity

Experimentally observed inelastic intensities due to single phonon scattering can be compared with the differential reflection coefficient $d^2R/dE_f d\Omega_f$, which is defined as the probability that a particle impinging on the surface is scattered with final energy E_f into the solid angle Ω_f. The differential reflection coefficient calculated with a potential obtained by a summation of pairwise interaction between the impinging particle and the surface atoms is given by [103, 108, 109],

$$\begin{aligned}\frac{d^2R}{dE_f d\Omega_f} &= \frac{L^4}{(2\pi\hbar)^3}\frac{m^2|\mathbf{k}_f|}{k_{iz}}\frac{2\pi S_{u.c.}}{\hbar}|v_0\langle k_{fz}|e^{-\beta z}|k_{iz}\rangle|^2 e^{-\frac{Q^2}{Q_c^2}} e^{-2W} \\ &\cdot \sum_{\alpha\alpha'}^{3} q_\alpha q_{\alpha'}^* [\rho^{\alpha,\alpha'}(-\mathbf{Q},\omega)n^+(\mathbf{Q},\omega) + \rho^{\alpha,\alpha'}(\mathbf{Q},\omega)n^-(\mathbf{Q},\omega)], \end{aligned} \tag{2.26}$$

where $\rho^{\alpha,\alpha\prime}(\pm\mathbf{Q},\omega)$ is the phonon spectral density, $v_0 e^{-\beta z}$ is the repulsive part of the atomic pair potential (Born-Mayer potential), and $\mathbf{q} = (i\mathbf{Q}, \beta)$.

The term $e^{-\frac{Q^2}{Q_c^2}}$ represents the "cut-off factor". Single phonon excitation by He atoms is limited to certain values of frequencies and momentums ("cut-off" effect) because He atoms, which are rather heavy and slow as compared to other probes like electrons, cannot excite phonons with high energy and short wavelength. Quantum mechanically, the cut-off is not absolute but characterized by a rapid decay of single phonon intensity. The cut-off frequency Q_c and the cut-off momentum $\hbar\omega_c$ for He scattering are typically $Q_c = 2$ Å and $\hbar\omega_c = 30 - 50$ meV [110]. The term ω_c is accounted for in the spectral density term $\rho^{\alpha,\alpha\prime}(\pm\mathbf{Q},\omega)$.

The temperature dependence of inelastic intensity is reflected by two terms, the Bose factor [93],

$$n^{\pm}(\mathbf{Q},\omega) = \frac{1}{2}[\coth\frac{\hbar\omega}{2k_BT} \pm 1], \tag{2.27}$$

(+ and - denote phonon creation and annihilation, k_B is the Boltzmann constant), and the Debye-Waller factor,

$$2W = 24\frac{m}{M}\frac{E_{iz}}{k_B\theta_D}\frac{T}{\theta_D}, \tag{2.28}$$

where θ_D is the surface Debye-temperature, E_{iz} the energy corresponding to the z-component of the incident wavevector, T the surface temperature, and M the mass of surface atoms. Single phonon scattering is dominant over multiple phonons if $2W < 1$ [111].

2.1.3 Surface Phonons and Time-of-flight Technique

Since surface atoms have fewer neighbors than the bulk atoms, the restoring forces of surface atoms are different from those of bulk atoms. One should thus normally expect the vibration of surface atoms to have different frequencies than those of bulk atoms. The surface vibration states lie either in the surface-projected bulk band-gap or are degenerate with the bulk states. Different vibration modes have been identified on crystal surfaces (see [112] for review). One of them is the Rayleigh mode. The Rayleigh waves propagate along the surface with the polarization vector (direction of displacement of atoms) lying in the sagittal plane (the plane defined by the surface normal and propagation direction of the wave). In the Rayleigh mode, the displacement of atoms decays exponentially with distance from the surface into the bulk. At the long wave length limit, the frequency of Rayleigh waves propagating along a given direction is proportional to the length of its 2D wave vector in the surface plane. The Rayleigh mode was first predicted

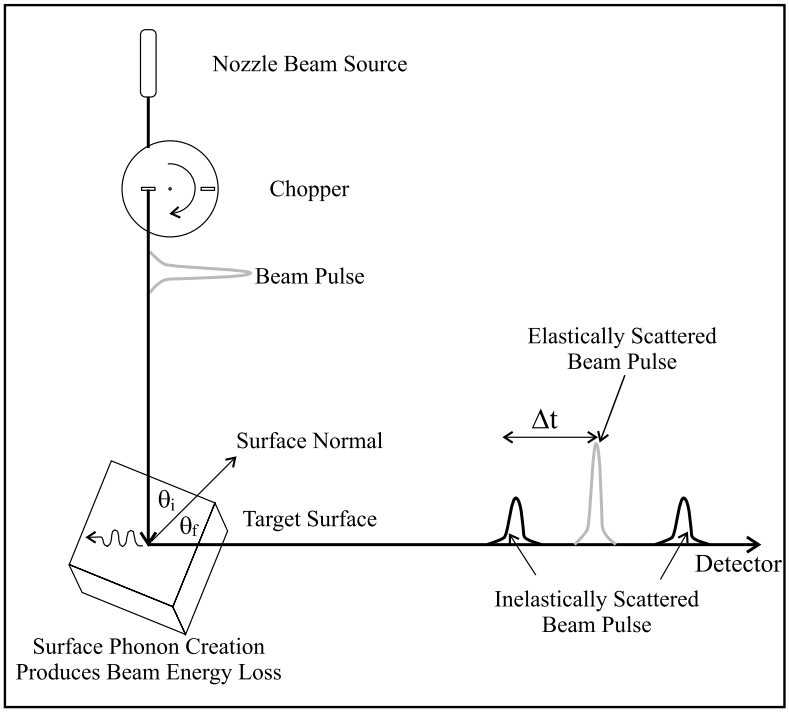

Figure 2.6: A schematic diagram of a surface phonon measurement using inelastic He scattering with time of flight analysis.

by Lord Rayleigh in 1887 on a semi-infinite, isotropic, elastic medium [113].

Since the Rayleigh modes are well separated from the bulk modes and the energy and momentum of these modes match those of He atoms, study of these modes by inelastic He scattering is possible. The time-of-flight (TOF) technique is used to measure the surface phonon dispersion. A schematic diagram of the TOF setup is shown in Figure 2.6. A highly monochromatic He beam is pulsed by a mechanical chopper and scattered from the sample surface. The inelastically scattered He atoms gain (or lose) energy due to phonon annihilation (or creation) and cause time-shifted peaks at the detector. The energy and parallel momentum exchanges (ΔE and ΔK) corresponding to inelastic phonon peaks is calculated from the time shift $\Delta t = t - t_e$ (t_e being the chopper-to-detector elastic flight time) and other experimental parameters. ΔE and ΔK can be expressed as,

$$\Delta E = E_i[(1 + \frac{d_{cd}\Delta t}{d_{td}t_e})^{-2} - 1], \tag{2.29}$$

and

$$\Delta K = k_i[(1 + \frac{d_{cd}\Delta t}{d_{td}t_e})^{-1}\sin\theta_f - \sin\theta_i], \tag{2.30}$$

where d_{cd} is the chopper-to-detector distance and d_{td} is the target-to-detector distance. A full set of points in $(\Delta E, \Delta K)$ space (a dispersion curve) is obtained by taking a set of spectra at different scattering angles θ_i and/or different He energies E_i.

The measured TOF spectra (intensity versus flight time) sometimes have to be converted into energy spectra (intensity versus energy exchange). The conversion always distorts the shape of the spectra because of the nonlinear relation of t and ΔE (see Equation 2.29). The creation peaks are more pronounced than annihilation peaks in the energy spectra (see [93, 114] for the derivation of scaling factors).

2.1.4 Experimental Setup

A schematic view of the experimental chamber used for the present work is shown in Figure 2.7 and important parameters of the apparatus are listed in Table 2.1. A He beam generated in the source chamber is directed towards the scattering chamber (SC) and the beam scattered from the surface of the sample is detected by a mass spectrometer. The angle between the incoming and outgoing beam is fixed at 90° and the parallel momentum transfer is probed by rotating the sample normal to the scattering plane. A brief description of the three main parts, the source

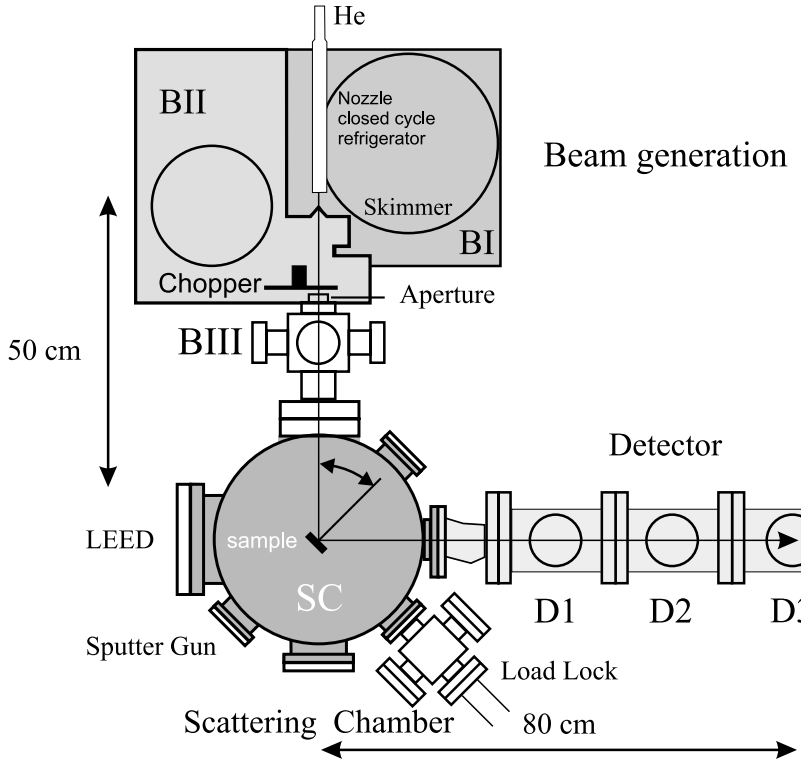

Figure 2.7: A schematic drawing of experimental chamber for He diffraction (B1 : expansion chamber, BII: chopper chamber, SC : scattering chamber, DI-DII : detector chambers).

chamber, the scattering chamber, and the detector chamber is presented below.

Source Chamber: A highly monochromatic He beam is produced by supersonic free jet expansion from a high pressure (10-100 bar) He gas through a tiny nozzle with a diameter 5 μm. During expansion, the randomly distributed velocities of atoms are converted into a uniform velocity v_s directed radially outward from the nozzle. The energy of the beam is determined by the nozzle temperature T_0,

$$\frac{1}{2}mv_s^2 = \frac{5}{2}k_BT_0. \tag{2.31}$$

The typical experimental range of T_0 is 30-300 K (v_s = 600-1800 m/s, λ_i = 1.4-0.6 Å). The lower temperature is achieved by a He refrigerator attached to the source. The full-width at half-maxima (FWHM) of the velocity distribution centered at v_s is determined by a characteristic speed ratio S defined by,

$$S = \frac{\frac{1}{2}mv_s^2}{k_BT} = \sqrt{\frac{5T_0}{2T}}, \tag{2.32}$$

where T is the temperature of thermal motion of the atoms in the beam, which ideally turns to zero due to the supersonic expansion. The FWHM (Δv) is related to S by [115],

$$\frac{\Delta v}{v_s} \sim \frac{1.65}{S}. \tag{2.33}$$

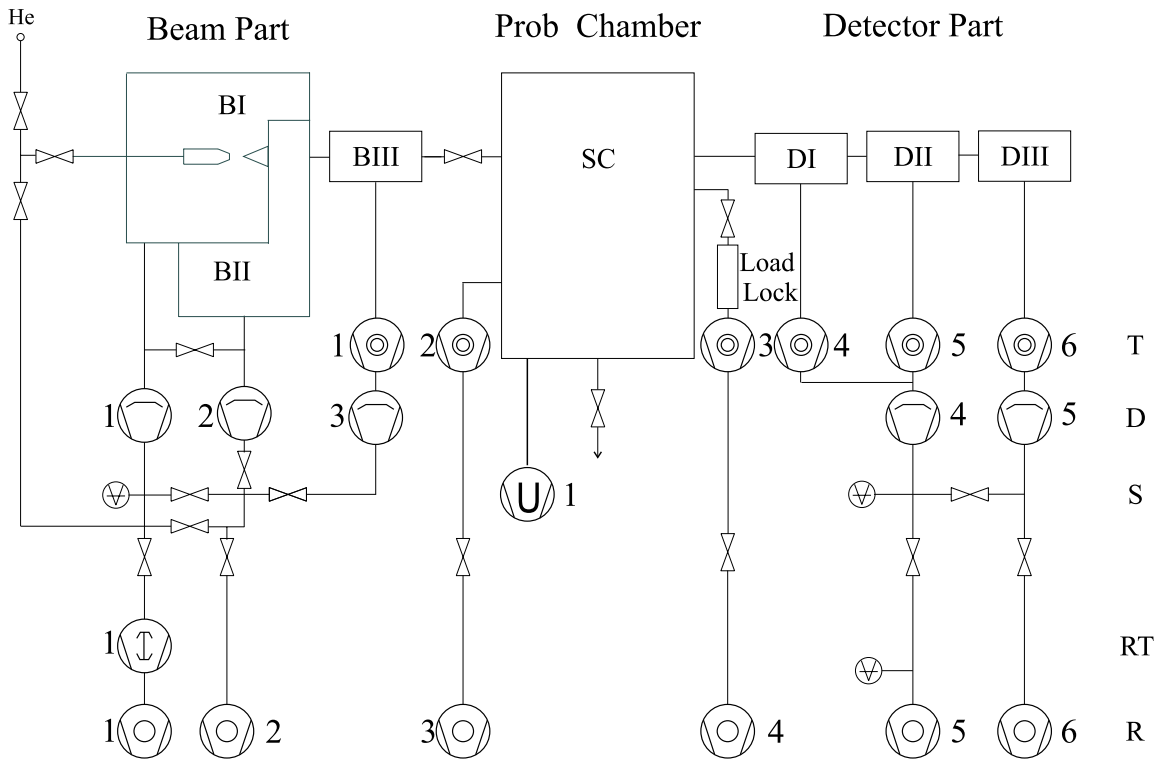

Figure 2.8: A schematic drawing of the vacuum system used in the He diffraction chamber shown in Figure 2.7. (T : turbo pump, D : diffusion pump, S : sublimation pump, RT : root pump, and R : rotary pump).

The value of S depends on the stagnation pressure P_0 and nozzle diameter d. Therefore, for an optimal velocity resolution, a system with a suitable combination of pressure, nozzle diameter and pumping speed is needed. The value of $\Delta v/v_s$ with the experimental parameters listed in Table 2.1 is $\sim 2\%$.

The monochromatic beam is collimated by a skimmer and then passed though an aperture (normally 0.6 mm) to achieve the angular resolution. The beam is then passed though the differential pumping units, which further reduces the undesired components of helium. For the time of flight measurements, the collimated beam is pulsed by a chopper before entering into the scattering chamber (chopper chamber: BII in Figure 2.7).

The He beam produced by this method has a disadvantage. Its velocity distribution contains a broad [93, 114], very low intensity tail with Maxwellian distribution, which creates a problem in the phonon measurements. The He atoms from the tail yield elastic diffraction peaks which appear in the TOF spectra as additional peaks. These peaks are called deceptons [93, 114]. Since

the intensity of these peaks is often comparable to that of the phonon peaks, it is difficult to distinguish them from the true phonon peaks without calculation. With the known experimental parameters, these peaks can be explicitly evaluated (see [93, 114]).

Scattering Chamber: The scattering chamber is equipped with the devices necessary to prepare and characterize the surface, such as LEED and a sputter gun. An ultra high vacuum is maintained (base pressure 2×10^{-10} mbar) in the chamber with high speed pumps and the residual gas is monitored by a mass spectrometer. The chamber is fitted with a manipulator which has three rotational degrees of freedom (θ, ϕ, and tilt) and three translation degrees of freedom (x, y, and z). The sample can be mounted on the manipulator through a load lock. The use of the load lock avoids the need to bake the chamber each time after mounting a new sample.

Detector Chamber: The detector chamber consists of three differential pumping stages. The differential pumping stages are used to reduce the He partial pressure. The detector chamber provides a longer flight path for the scattered atoms yielding a better energy resolution of the time of flight spectra. The scattered He atoms are ionized by an electron bombardment ionizer prior to entering into the mass spectrometer. The mass spectrometer signal is amplified by an electron multiplier and is fed to the computer.

Transfer Width and Time-of-flight Resolution

In diffraction experiments, the width of diffraction peaks is limited by the transfer width (W) of the apparatus. For the scattering geometry shown in Figure 2.3, W can be expressed as [95, 116],

$$W = \frac{\lambda}{\sqrt{(\Delta_\theta \cdot \theta_f)^2 \cos^2\theta_f + (\sin\theta_i - \sin\theta_f)^2 \frac{(\Delta E)^2}{E^2}}}, \tag{2.34}$$

where Δ_θ is the angular spread due to the source and the detector and $(\Delta E)^2$ is the energy spread. For the specular beam ($\theta_i = \theta_f$), the energy spread term vanishes such that it does not contribute in the broadening of the specular peak. With the experimental parameters listed in Table 2.1, the transfer width of our instrument is ~ 100 Å.

In a time-of-flight measurement, the total flight time t_{tof} is the sum of the contributions coming from four different parts of the apparatus,

$$t_{tof} = t_{chop} + t_{ct} + t_{td} + t_{ion}, \tag{2.35}$$

Source	Nozzle diameter	5 μm
	Nozzle pressure	$\leq$ 100 bar
	Nozzle temperature	30-300 K
	He beam energy	10-65 meV
	He beam velocity	600-1800 m/s
	Relative velocity spread ($\Delta v/v_s$)	$\sim$ 2%
Chopper	Slit diameter	15-17 cm
	Slit width	0.5 mm
	Disk rotational frequency	$\sim$ 80 Hz
	Shutter function	$\sim$ 12 μs
	Number of slits	8
Dimensions	Source-target distance	$\sim$ 50 cm
	Target-detector distance	79.8 cm
	Chopper-target distance	35.8$\pm$0.2
	Source-target-detector angle (fixed)	90$\pm$0.25°
Detector	Ionization volume	15$\times$7.5$\times$11 mm^3
	Channel width MCA	1μs
	Dynamic range	$\sim 5 \times 10^5$
Resolution	Polar angle	$\sim$ 0.25°
	Energy resolution	$\sim \pm$ 0.2 meV
	Transfer width	$\sim$ 100 Å
Pressure	Source (expansion) chamber (BI)	10^{-7} mbar (without helium)
		10^{-4} mbar (with helium)
	Chopper chamber (BII)	10^{-8} mbar (without helium)
		10^{-6} mbar (with helium)
	Scattering chamber (PC)	10^{-10} mbar (without helium)
		10^{-9} mbar (with helium)
	Detector chamber (DI-DIII)	10^{-10} mbar (without helium)
		10^{-10} mbar (with helium)

Table 2.1: A list of important experimental parameters.

where the first term is a finite opening time of the chopper slit, t_{CT} the flight time from chopper to target, t_{td} the flight time from target to detector, and the last term is the time lapses by He atoms in the ionizer before detection. All four terms contribute in the broadening of phonon peaks. The overall spread in time can be calculated by [93],

$$\Delta t_{tof} = \sqrt{\Delta t_{chop}^2 + \Delta t_{ct}^2 + \Delta t_{td}^2 + \Delta t_{ion}^2}. \tag{2.36}$$

All terms except the third one can be simply calculated from the dimensions of the apparatus. The third term is associated with energy and angular spread (refer to [93, 110, 117] for detail). From the total time spread Δt_{tof}, the total energy width can be obtained by,

$$\delta(\Delta E) = \frac{\partial \Delta E}{\partial t_{tof}} \Delta t_{tof} = -2E_i(1 + \frac{\Delta E}{E_i})^{3/2} \frac{\Delta t_{tof}}{t_{cd}^e}. \tag{2.37}$$

This implies that the energy width of phonon peaks in a spectrum is narrower for the creation peaks ($\Delta E < 0$) than the annihilation peaks ($\Delta E > 0$) provided that Δt_{tof} is similar for $\Delta E < 0$ and $\Delta E < 0$.

2.2 Spot Profile Analyzing Low Energy Electron Diffraction

Kinematics Approximation of Low Energy Electron Diffraction

The de Broglie wave length of electrons is related to the incident energy E_i by

$$\lambda_i/\text{Å} = \sqrt{\frac{150.4}{E_i/\text{eV}}}. \tag{2.38}$$

In diffraction experiments, normally electrons with energies of 50-200 eV ($\lambda_i = 1.7 - 0.8$ Å) are used. The mean free path of the electrons in this energy range is a few Angstroms, such that the electrons penetrate a few atomic layers into the solid and undergo multiple scattering (see Figure 2.1). Therefore, one has to consider these multiple scattering events explicitly to evaluate the diffraction intensities. The kinematic approximation, which considers only single scattering, yields part of the information of the LEED pattern, namely the size and symmetry of the unit cell [118, 119].

Consider electrons with initial wave vector $\mathbf{k}_i$ scattered from the surface with final wave vector $\mathbf{k}_f$. Assuming the incoming and outgoing electrons as plane waves, the diffraction from

the surface is normally described by a sum of scattered wave functions by all surface atoms at position $\mathbf{r}_n$ [120],

$$\psi(\mathbf{k}, \mathbf{k}_i) = \sum_n f_n(\mathbf{k}, \mathbf{k}_i) e^{i\mathbf{k}\mathbf{r}_n}, \tag{2.39}$$

where $\mathbf{k} = \mathbf{k}_i - \mathbf{k}_f$ is the scattering vector and $f_n(\mathbf{k}, \mathbf{k}_i)$ is the structure factor, which combines the electron waves coming from the surface atom at $\mathbf{r}_n$ and all atoms of the underlying column.

The diffraction intensity is calculated by,

$$I(\mathbf{k}, \mathbf{k}_i) = |\psi(\mathbf{k}, \mathbf{k}_i)|^2 = \sum_{n,m} f_m(\mathbf{k}, \mathbf{k}_i) f_n^*(\mathbf{k}, \mathbf{k}_i) e^{i\mathbf{k}(\mathbf{r}_n - \mathbf{r}_m)}. \tag{2.40}$$

Within the kinematic approximation, all structure factors $f_n(\mathbf{k}, \mathbf{k}_i)$ are replaced by an identical structure factor $f(\mathbf{k}, \mathbf{k}_i)$ so that these factors can be taken out of the summation. Then, the intensity $I(\mathbf{k}, \mathbf{k}_i)$ simply splits up into two factors

$$I(\mathbf{k}, \mathbf{k}_i) = F(\mathbf{k}, \mathbf{k}_i) G(\mathbf{k}), \tag{2.41}$$

with the dynamical form factor

$$F(\mathbf{k}, \mathbf{k}_i) = |f(\mathbf{k}, \mathbf{k}_i)|^2, \tag{2.42}$$

and the lattice factor or interference factor,

$$G(\mathbf{k}) = \sum_{n,m} e^{i\mathbf{k}(\mathbf{r}_n - \mathbf{r}_m)}. \tag{2.43}$$

The dynamical form factor $F(\mathbf{k}, \mathbf{k}_i)$ contains the information of the arrangement of atoms within the unit cell and multiple scattering events of all kinds, whereas the lattice factor $G(\mathbf{k})$ includes the information on arrangement of unit cells. Since the lattice factor $G(\mathbf{k})$ depends only on the scattering vectors $\mathbf{k}$ and the position vectors $\mathbf{r}_n$, it can be easily calculated. Thus, the kinematic approximation is sufficient to determine the arrangement of scattering units.

Experimental Details of Spot Profile Analyzing Low Energy Electron Diffraction

An instrument for quantitative spot profile analysis of low energy electron diffraction (SPA-LEED) was developed by Scheithauer *et al.* in 1986 [121]. A schematic view of a SPA-LEED is shown in Figure 2.9. An electron beam generated by an electron gun is scattered from the sample surface and detected by a Channeltron single electron detector. The incident angle of the electron beam is varied by using an electrostatic deflection unit, as opposed to rotating the

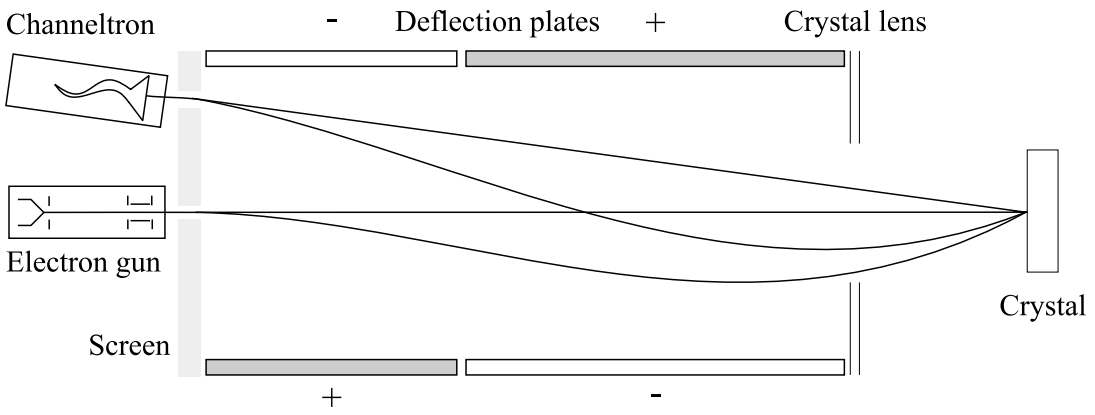

Figure 2.9: A schematic drawing of spot profile analyzing low electron diffraction instrument.

sample or detector. The geometrical angle between the electron gun and the detector is fixed at 4°. The instrument is also equipped with a florescent screen as in the case of conventional LEED apparatus.

The SPA-LEED instrument has many advantages over conventional LEED. A dynamic range of 10^6 is achieved by the use of a Channeltron. Employing an electrostatic field, the angle of incidence can be varied more smoothly than in the case of mechanical rotation of the sample or detector. A determination of the lattice parameter with an accuracy of up to 0.02 Å is possible. Because of the large transfer width of the instrument, morphological features can be determined up to a scale of 2000 Å [120]. Since the scattering geometry fixes the angle between incident and final wave vectors, variation of the incident angle rotates the Ewald sphere around the origin of the reciprocal space. The radius of the modified Ewald sphere (sphere with solid boundary line in Figure 2.4(b)) is twice the radius of the Ewald sphere. The larger diameter of the modified Ewald sphere, in principle, offers a larger area of reciprocal space accessible to the measurements.

For the present work, a commercial Omicron SPA-LEED (transfer width larger than 1000 Å, angular spread at 95 eV of 0.08° and energy resolution of 0.1 eV) was used.

2.3 Scanning Tunneling Microscopy

Technical Basic

The scanning tunneling microscope uses an atomically sharp, normally metallic tip. The tip is mounted on a system of piezoelectric drives, which allows controlled movements in three directions with an accuracy on an atomic scale and is brought very close to the surface under investigation. At a separation of a few Angstroms, the electronic states close to the Fermi level of the sample and of the tip overlap. Upon application of a small bias voltage (V) between the tip and the sample, electrons start to tunnel though the vacuum barrier due to the quantum mechanical tunneling effect. The tunneling current I_T depends exponentially on the tip-surface separation d. For a small bias voltage and low temperature, I_T is

$$I_T \propto \frac{V}{d} e^{-2kd}, \tag{2.44}$$

where $2k/\text{Å}^{-1} = 1.025\sqrt{\phi/eV}$, with ϕ the average work function of sample and tip [100]. The exponential dependence implies that the tunneling current is extremely sensitive to the tip-sample separation, which provides a high resolution perpendicular to the surface (up to hundredths of an Ångstrom).

The scanning tunneling microscope can be operated in two modes, the constant current mode and the constant height mode. In constant current mode, the tip is scanned across the surface with constant tunneling current. The constant current is maintained during scanning by using an electronic feedback loop, which adjusts the vertical distance between the tip and the surface with a feedback voltage. The feedback voltages is plotted as a function of the lateral scan position in a computer, mapping the surface morphology. In constant height mode, the tip is moved in a horizontal plane above the surface and the tunneling current is recorded. This mode of scan is faster than the constant current mode providing an opportunity to study dynamical processes on the surface. However, this mode is only applicable for atomically flat surfaces because scanning with constant height on rough surfaces crashes the tip.

Theoretical Basis

The tunneling current can be evaluated within Bardeen's formalism [100],

$$I_T = \frac{2\pi e}{\hbar} \sum_{\mu\nu} [f(E_\mu)\{1 - f(E_\nu + eV)\} - f(E_\nu + eV)\{1 - f(E_\mu)\}] |M_{\mu\nu}|^2 \delta(E_\mu - E_\nu), \tag{2.45}$$

where $f(E)$ is the Fermi function, V sample bias voltage, $M_{\mu\nu}$ the tunneling matrix element between the unperturbed electronic states of the tip ψ_μ and those of the sample ψ_ν, and E_μ (E_ν) the energy of the state ψ_μ (ψ_ν). The matrix element $M_{\mu\nu}$ can be obtained as

$$M_{\mu\nu} = \frac{\hbar^2}{2m} \int (\psi_\mu^* \Delta\psi_\nu - \psi_\nu \Delta\psi_\mu^*) \cdot d\mathbf{S}. \tag{2.46}$$

The matrix element can be derived explicitly if the wave functions of tip and the surface are known. But, the shape of the tip is unknown in practice. Therefore, a model wave function of the tip has to be assumed. Further explanations of the model tip wave functions and the derivation of the tunneling current are given in Ref. [100].